








Directional seismic response to the complex topography: A case study of 2013 Lushan Ms 7.0 earthquake

ZHAO Bo^{1,2*}  <https://orcid.org/0000-0002-2565-8752>;  e-mail: zhaobo1989@imde.ac.cn

WANG Yun-sheng^{2*}  <https://orcid.org/0000-0002-1774-9494>;  e-mail: wangys60@163.com

SU Li-jun^{1,3,4,5}  <https://orcid.org/0000-0001-9972-4698>; e-mail: sulijun1976@163.com

LUO Yong-hong²  <https://orcid.org/0000-0001-7462-1182>; e-mail: lyh445890689@qq.com

ZHANG Jing²  <https://orcid.org/0000-0002-2634-8561>; e-mail: 244207394@qq.com

*Corresponding author

¹ Key Laboratory of Mountain Hazards and Earth Surface Processes, Institute of Mountain Hazards and Environment, Chinese Academy of Sciences, Chengdu 610041, China

² State Key Laboratory of Geohazard Prevention and Geoenvironment Protection, Chengdu University of Technology, Chengdu 610059, China

³ CAS Center for Excellence in Tibetan Plateau Earth Sciences, Beijing 100101, China

⁴ China–Pakistan Joint Research Center on Earth Sciences, Islamabad 30001, Pakistan

⁵ University of Chinese Academy of Sciences, Beijing 100049, China

Citation: Zhao B, Wang YS, Su LJ, et al. (2020) Directional seismic response to the complex topography: A case study of 2013 Lushan Ms 7.0 earthquake. *Journal of Mountain Science* 17(9). <https://doi.org/10.1007/s11629-020-6038-y>

© Science Press, Institute of Mountain Hazards and Environment, CAS and Springer-Verlag GmbH Germany, part of Springer Nature 2020

Abstract: Azimuthal variations in site response can provide a good insight into the site amplification and seismic conditions of geohazard occurrences. In this study, multiple directional site response methods, including D-Arias (Directional-Arias), D-SER (Directional-Shaking energy ratio), D-HVSR (Directional-Horizontal to vertical spectral ratio) and D-SSR (Directional – Standard spectral ratio), are adopted to analyse seismic data of the 2013 Lushan Ms 7.0 earthquake captured by the self-established Lengzhuguan (LZG) station which consists of the complex topography of isolated ridge, large mountain and some typical micro-reliefs. The results show that the isolated ridge could cause stronger site responses than the large mountain, and whose pronounced response direction is roughly perpendicular to its ridgeline. With the growth of elevation, the site

resonant frequency decreases. The different micro-reliefs on the mountain cause different site responses, which present as protruding slope > linear slope. The site response mainly exists on the surficial layer of the mountain and shows that with the increase of the distance to mountain surface, the site response gets weaker, the site resonant frequency gets higher, and the pronounced response direction is perpendicular to its ridgeline.

Keywords: Site response; Pronounced response direction; LZG station; Lushan Ms 7.0 earthquake

Introduction

In recent years, earthquakes, especially strong earthquakes, have caused numerous catastrophic consequences worldwide by triggering numerous geohazards, such as landslides and rock avalanches,

Received: 21-Feb-2020

1st Revision: 17-Apr-2020

2nd Revision: 16-May-2020

Accepted: 09-Jun-2020

which have buried villages and blocked roads and rivers; for example, the 2008 Wenchuan Ms 8.0 earthquake triggered 197,481 landslides, which caused thousands of deaths and dammed 828 lakes (Xu et al. 2013a; Fan et al. 2012). Therefore, the dynamic responses of slope stability under seismic shaking have attracted the attention of many scholars (Gaudio and Wasowski 2007, 2011; Gaudi et al. 2008, 2014, 2015; Luo et al. 2013, 2014; Wang et al. 2017; Zhao et al. 2018).

Topographic amplification, as an important component of slope dynamic responses, has been viewed as an important landslide trigger during earthquakes based on the peak ground acceleration ratio distributions at different hill heights and the relationships between landslide distributions and topographic reliefs (Harp and Jibson 2002; Sepúlveda et al. 2005; Zhao et al. 2018, 2019, 2020). To quantitatively analyse site responses, Arias (1970) proposed the Arias Intensity, which is defined as the integral of the energy per unit weight of the local ground motion caused by an earthquake, to characterize the scale of seismic shaking energy; Borcherdt (1970) proposed a spectral ratio between a targeted seismic site and reference seismic site, named the SSR (standard-spectral-ratio), to analyse site response intensities; and Nakamura (1989) proposed a self-spectral ratio of the horizontal and vertical spectra, which was named HVSR (horizontal-to-vertical-spectral-ratio). HVSR was first applied to the analysis of ambient noise. Additionally, Lermo and Chavez (1993) adopted HVSR to analyse seismic responses.

These seismic data processing methods have been widely used to determine site response properties. For example, monitoring data captured by Geli et al. (1988) shows that site amplification of S waves is more intense than site amplification of P waves. Pedersen (1994) established a seismic station on the same hill, and the monitoring data shows that with increased elevation, the site response is more intense, while similar results have been obtained by other scholars (Wang et al. 2012, Tripe et al. 2013, Parker et al. 2015). Luo et al. (2013) performed a preliminary analysis of site amplifications of different geomorphic units (e.g., isolated ridge and large mountain) and elevations of the Lengzhuguan station induced by the 2013 Lushan Ms 7.0 earthquake. Ashford and Sitar (1997) placed an accelerometer on loose deposits and

determined that loose deposits could cause more intense site responses than the nearby bedrock; Zhao et al. (2018) also obtained similar results in aftershock monitoring of the 2017 Jiuzhaigou Ms 7.0 earthquake. In addition, several numerical simulations have noted that the impedance contrasts between surface materials and underlying substrata are possible causes of site amplification, which favour landsliding (Bourdeau and Havenith 2008; Fiore 2010).

Actually, the propagation directions of the seismic wave and lithological characteristics allow simple analyses of site amplification that do not consider anisotropic effects, leading to an inaccurate reflection of the dynamic characteristics of slope instability (Spudich 1996; Gaudio and Wasowski 2007; Gaudio et al. 2008, 2015; Pischitta et al. 2012; Panzera et al. 2017). Anisotropic amplification provides new insights into the seismic conditions of slope failure, and such phenomena have been observed in the Caramanico area of Italy (Gaudio et al. 2007). These observations have been interpreted as the effects of azimuthal resonance, which generates anisotropic site amplification, while its cause is still unclear. This study adopts polarization processing methods to analyse anisotropic amplification considering the topographic and lithological characteristics of the Lushan seismic data, which were captured by the self-built Lengzhuguan station located along the upstream part of the Dadu River, China.

1 Study Area and Seismic Events

1.1 Regional setting

It is widely accepted that the lateral extrusion of the Tibetan Plateau was resisted by the rigid Sichuan Basin to the east, which resulted in the uplift of the eastern boundary of the Bayan Har fault block and caused the eastern boundary of the Bayan Har fault block to be very active (Xu et al. 2017; Zhao et al. 2018). The self-built LZG station is at the intersection of three active fault block zones: the Sichuan Basin, Songpan-Ganzi block zone and Chuan-Dian block zone, and numerous large earthquakes are distributed along the block boundaries (Figure 1, Wang et al. 2011; Sun et al.

2018). Regional GPS measurements near the LZG station have shown obvious differences from greater than 10 mm/yr in the Chuan-Dian block to less than 6 mm/yr in the Sichuan Basin (Figure 1, Zhao et al. 2015). Two world-famous fault zones, namely, the Longmenshan fault zone, which triggered the 2008 Wenchuan Ms 8.0 earthquake and 2013 Lushan Ms 7.0 earthquake (Xu et al. 2009a; Gorum et al. 2011; Xu et al. 2013b), and the Xianshuihe fault zone, which has triggered numerous large earthquakes, such as the 1725 Kangding Ms 7.0 earthquake, 1786 Moxi Ms 7.75 earthquake and 1955 Zheduotang Ms 7.5 earthquake (Zhou et al 1983; Papadimitriou et al. 2014; Dai et al. 2005), also meet near the LZG station (Figure 1). The above observations indicate

that the area of the LZG station is in the most seismically active region of China, and thus, the LZG station is useful for capturing possible mega-earthquakes.

The LZG station sits on the right bank of the upstream portion of the Dadu River (Figures 1 and 2). The Dadu River, whose length exceeds 1000 km, passes through the LZG area and forms a typical deep-cutting gorge with a slope usually larger than 45° (Dai et al. 2005; Deng et al. 2017). High geostress, intense river incision, and frequent large earthquakes have caused the numerous giant landslides that have occurred in this region (Wu 2013; Zhao 2020).

The geological units in the LZG area are mainly Proterozoic granites. The frequent seismic events

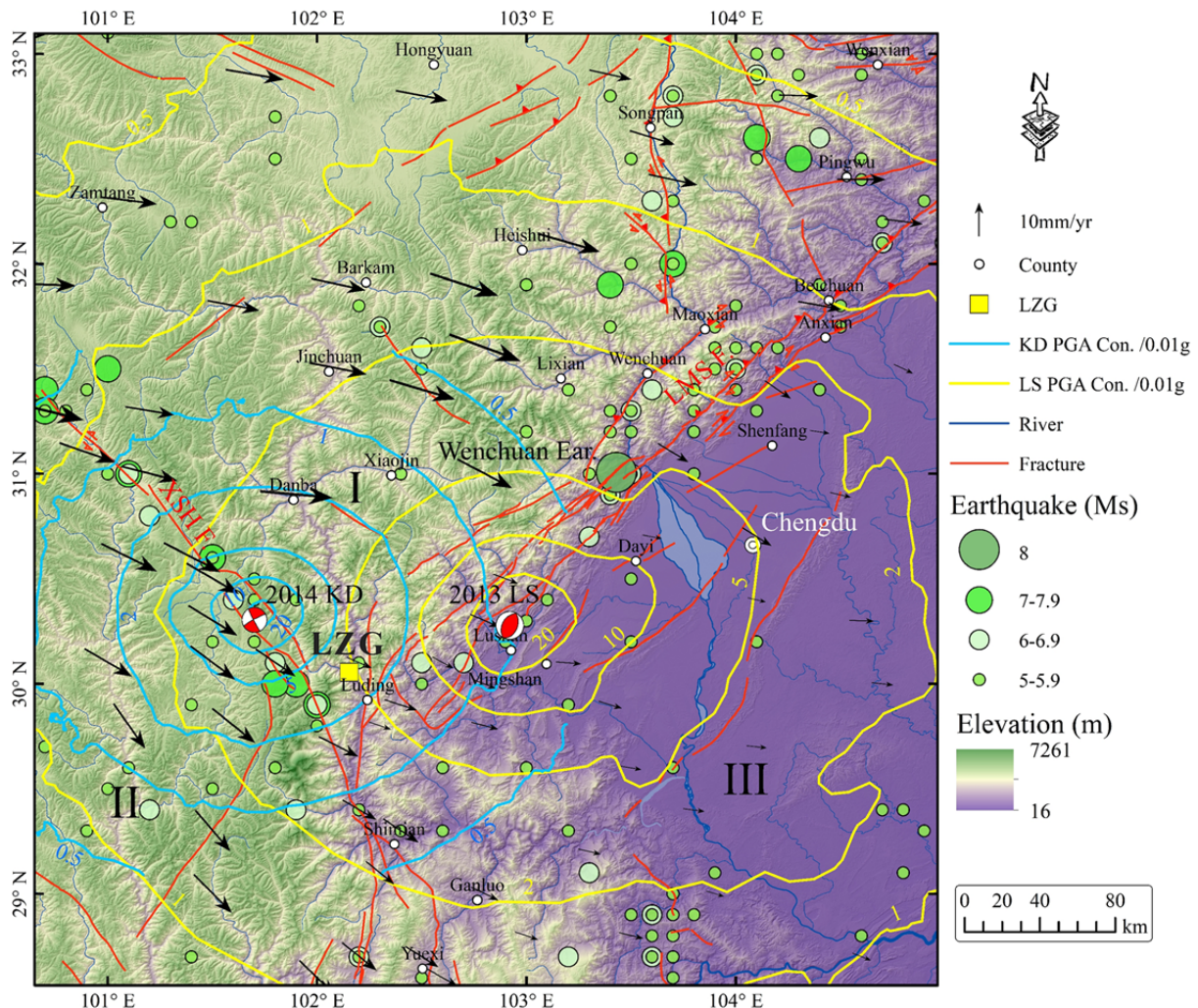


Figure 1 The location of Lengzhuguan (LZG) station in fault blocks, and the distribution of historical earthquakes. LS, Lushan, KD, Kangding; I- Songpan-Ganzi fault block, II- Chuan-Dian fault block, III- Sichuan basin; XSH F. – Xianshuihe fault zone, LMS F. – Longmenshan fault zone, LZG –Lengzhuguan station. The GPS data is from Zhao et al. 2015. The PGA (Peak Ground Acceleration) contours (Lushan event and Kangding event) are from USGS (2013, 2014).

and complex topographic units motivated the establishment of the LZG station in Lengzhuguan village, and the distance from the LZG station to Luding County is approximately 16 km.

1.2 Seismic events

(1) Lushan Ms 7.0 earthquake

On April 20, 2013, an Ms 7.0 earthquake (Lushan earthquake) struck Lushan County, Sichuan Province, China (Figure 2). The Lushan earthquake was a reverse-fault earthquake with a focal depth of 13 km located at 30.28°N and 102.95°E (Liu et al. 2013). The Lushan earthquake occurred along the SDF (the Shuangshi-Dachuan fault, which is a branch of the Longmenshan fault zone), which trends in a NE direction and whose length is approximately 35 km-40 km (Figure 2, Li et al. 2013; Tang et al. 2015); the Lushan event triggered more than 10 thousand geohazards (Xu et al. 2015). The epicentre was approximately 86 km

from the LZG station and was at a bearing of NE 72.6° relative to the LZG station.

Figure 2 shows the PGA distribution induced by the Lushan event, and the LZG station is just slightly outside of the PGA contour – 0.49 (0.05×9.8) m/s² (USGS 2013).

(2) Kangding Ms 6.3 earthquake

On November 22, 2014, an Ms 6.3 earthquake (Kangding earthquake) struck Kangding County, Sichuan Province, China (Figure 1). The Kangding earthquake was a strike-slip earthquake with a focal depth of 11 km located at 30.27°N and 101.69°E (Yi et al. 2015). The origin of the Kangding earthquake was the Zheduotang fault (which is a branch of the Xianshuihe fault zone, Yi et al. 2015), which trends in a SW direction and whose length is approximately 30 km (Yi et al. 2015). The epicentre was approximately 51 km from the LZG station and was at a bearing of N62.4°W relative to the LZG station. The LZG station was located within the PGA contour of 0.20

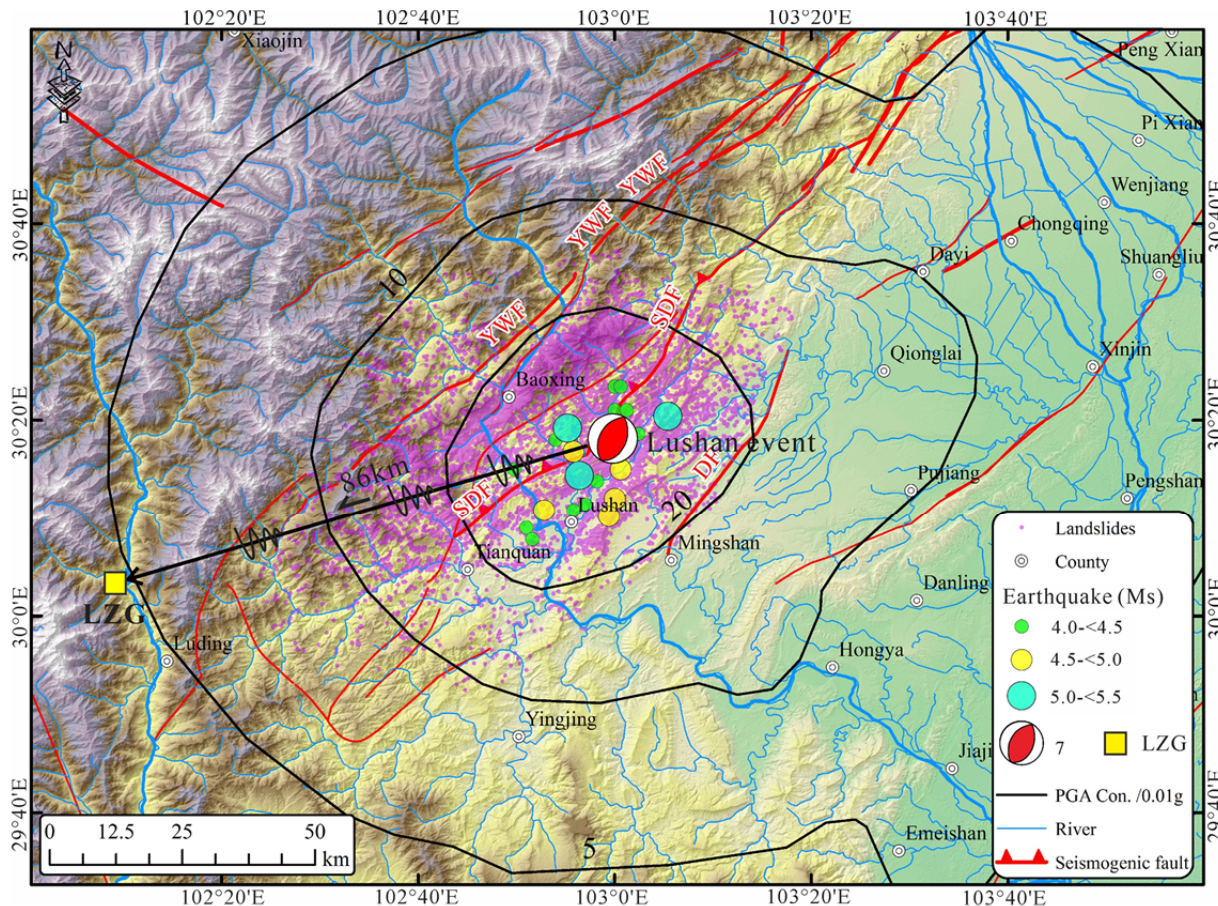


Figure 2 The basic information of Lushan event and its relative position relation with Lengzhuguan (LZG) station. YWF - Yanjing-Wulong fault, SDF - Shuangshi-Dachuan fault, DF - Dayi fault. The seismogenic fault is from Li et al. (2013), the PGA (Peak Ground Acceleration) contour is from USGS (2013). The landslide data is from Xu et al. (2015).

$(0.02 \times 9.8) - 0.49$ (0.05×9.8) m/s^2 (USGS 2014).

1.3 Lengzhuguan Seismic Station

There are seven accelerograph sites (e.g., L1-L7) at the LZG station distributed on both sides of the LZG valley. The local slopes consist of large gradients that are usually $> 40^\circ$ and have outcrops of Proterozoic granites (Figure 3).

The L2 (one accelerograph) and L1 (one accelerograph) sites are located in the middle and top parts of an isolated ridge on the right side of the Lengzhuguan valley, with elevations of 1478 m and 1516 m, respectively (Figures 3 and 4). The isolated ridge is referred to as a special ridge with multiple aspects (at least three directions among all four directions) facing free. Site L1 is 100 m above the Dadu River, the bedrock is granite, and the surface layer is medium weathered granite; two main joints (e.g., joint-1: $218^\circ \angle 56^\circ$, joint-2: $218^\circ \angle 56^\circ$) have developed, and Quaternary residual deposits are present (Figure 4A). Site L2 is 62 m above the Dadu River, the surface granites are fractured, and several Quaternary residual deposits

cover the bedrock (Figure 4A). To place the accelerograph (L2) on intact bedrock, an 8 m deep adit was excavated, and the accelerograph was placed at the end of the adit (intact bedrock).

Sites L3-L4 are located on a large mountain located on the left side of the Lengzhuguan valley (Figures 3 and 4). Site L3 (one accelerograph, elevation: 1494 m) is located on the valley bottom (it is out of service at present). Site L4 (one accelerograph) is located in the transition zone between gentle slopes (upper section $< 30^\circ$) and steep slopes (lower section $> 50^\circ$) and is 78 m above the Dadu River (Figure 4D). The bedrock consists of granite, and the surface layer is medium weathered granite; several Quaternary residual deposits cover the bedrock. A 10 m deep adit was excavated and the accelerograph is located at the end of the adit (intact bedrock).

Site L5 (one accelerograph, elevation: 1518 m) is located in a slope break section (the aspect changes rapidly) and is 102 m above the Dadu River (Figure 4C). The surface layer consists of medium weathered granite, and three primary joints (e.g., joint-1: $210^\circ \angle 18^\circ$, joint-2: $120^\circ \angle 78^\circ$,

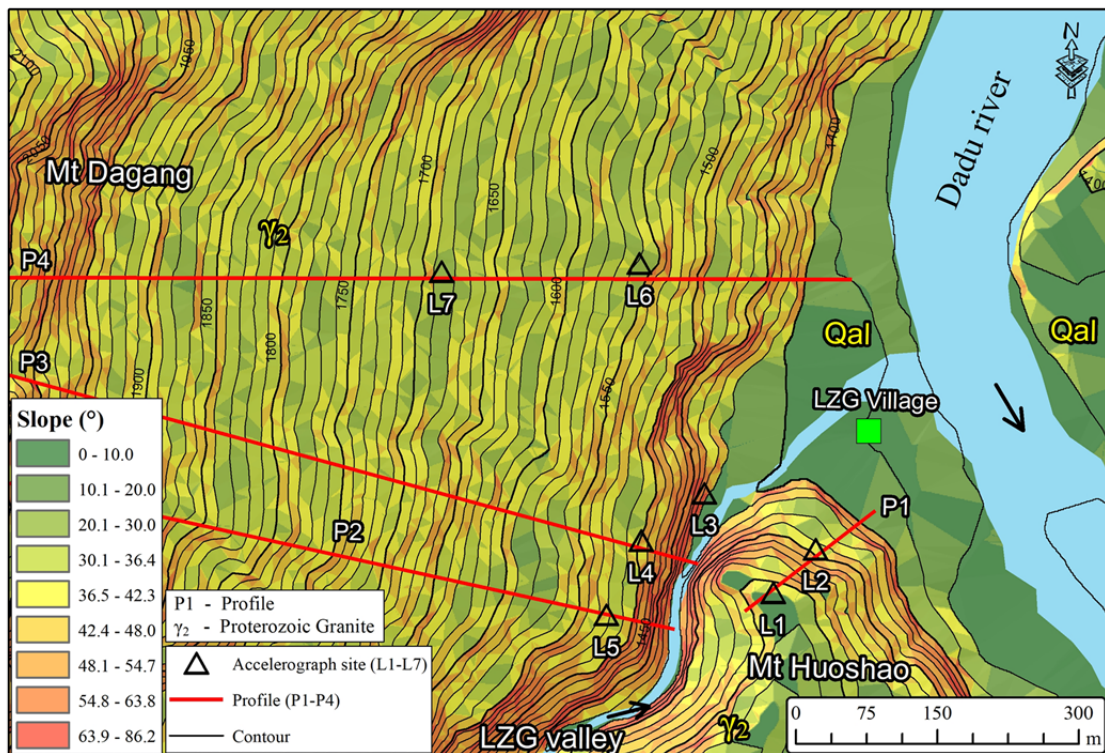


Figure 3 Detailed information of LZG station. A - The aerial view of LZG station on right bank of Dadu river, B - Topographic feature and slope distribution near LZG station. P1-P4 geological profiles are shown in Figure 5. Triangles L1 -L7 are accelerograph sites.

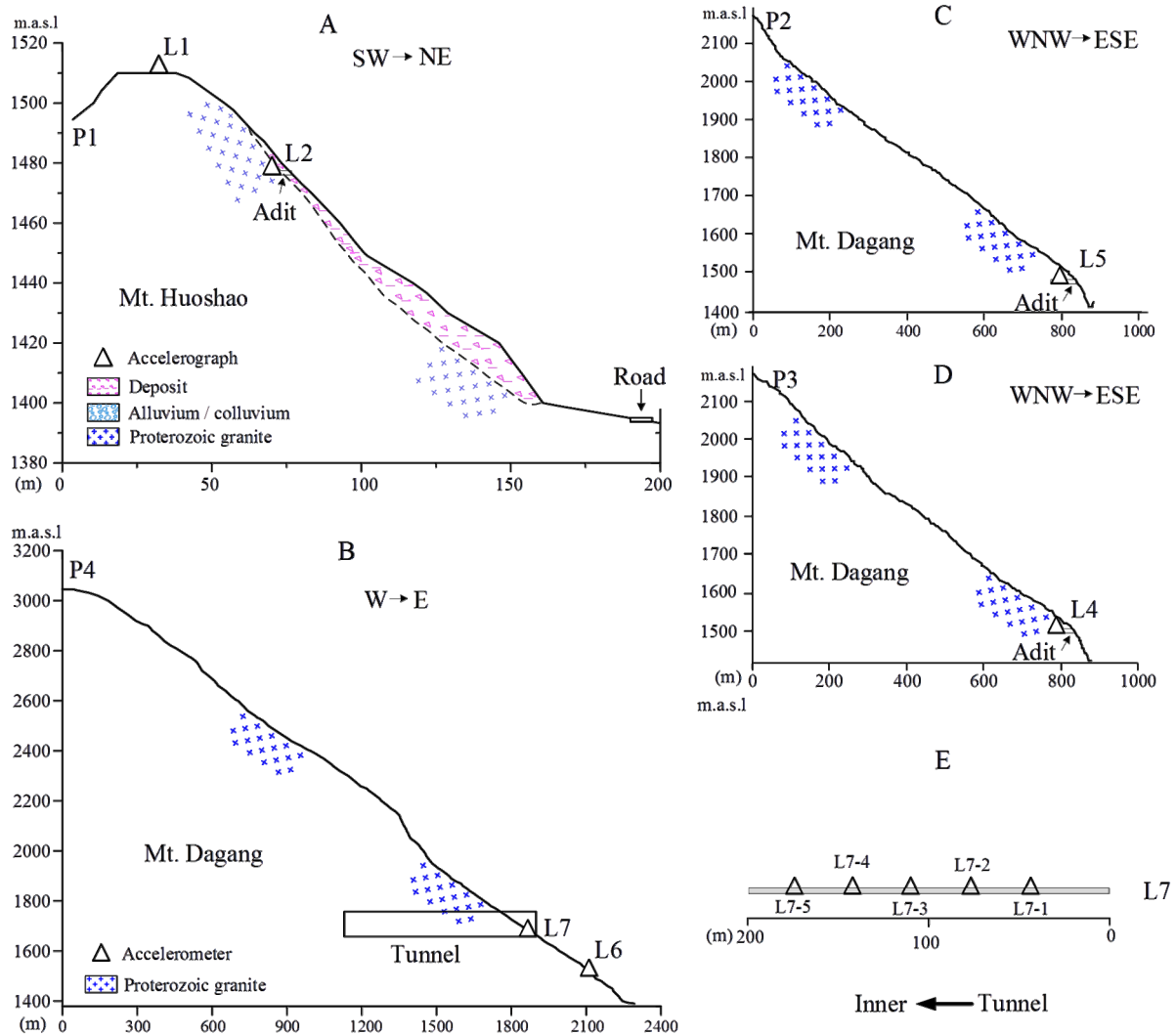


Figure 4 The topographic and geological profiles of Mt. Huoshao (A) and Mt. Dagang (B, C and D) slopes, and the accelerometer distribution in the diversion tunnel (site L7) (E). The locations are listed in Figure 3.

joint-3: $328^\circ \angle 72^\circ$) have developed. A 15 m deep adit was excavated, and the accelerograph was placed at the end of the adit (intact bedrock).

Site L6 (one accelerograph, elevation: 1520 m) is located on a nearby rectilinear slope and is 106 m above the Dadu River (Figure 4B). The surface layer consists of slightly weathered granite.

Site L7 (five accelerographs, elevation: 1686 m) is located in a diversion tunnel. There are five accelerographs whose intervals along this tunnel are approximately 50 m, while the outermost accelerograph is located approximately 50 m from the tunnel entrance (Figures 4B and 4E). The rock is intact granite.

According to site verifications, the 2013 Lushan event activated L1, L2, L4, L4, L6, L7-1 and

Table 1 Triggered information of all accelerographs by two earthquake events

Event	Accelerograph						
	1#	2#	4#	5#	6#	7#-1	7#-5
LS	7.0	7.0	7.0	7.0	7.0	7.0	7.0
KD	6.3	6.3	/	/	/	/	/

Note: LS, Lushan earthquake in 2013; KD, Kangding earthquake in 2014.

L7-5 and the 2014 Kangding event activated L1 and L2, as listed in Table 1. The basic seismic information of the Lushan event as captured by the LZG station is listed in Table 2.

For data processing and analysis, a reference accelerograph is necessary. The reference accelerograph should be located on stable and intact rock because it can produce weaker site

Table 2 Basic seismic information of all activated monitoring points (Lushan event)

Accelerograph	PGA (m/s ²)			Elevation (m)	Local topography	Mountain
	NS	EW	UD			
L1	1.538	1.635	0.667	1516	Top part	Isolated ridge
L2	0.393	0.424	0.290	1478	Middle part	Isolated ridge
L4	0.309	0.366	0.203	1494	Transition zone	Huge mountain
L5	0.218	0.303	0.250	1518	Slope break	Huge mountain
L6	0.146	0.112	0.155	1520	Linear slope	Huge mountain
L7-1	0.185	0.110	0.127	1686	Tunnel outer	Huge mountain
L7-5(L7R)	0.139	0.126	0.111	1686	Tunnel inner	Huge mountain

Note: PGA, peak ground acceleration. NS: North-South, EW: East-West, UD: Up-Down.

effects at this position (Borcherdt 1970; Spudich 1996); accelerograph L7-5 meets these requirements. Therefore, L7-5 was chosen as the reference accelerograph.

2 Methodology

To detect the directional site responses to slopes that were triggered by seismic events, several seismic data processing methods were adopted, including D (Directional)-Arias (Gaudio and Wasowski 2007), D (Directional)-HVSr (Horizontal-to-vertical spectral ratio) (Gaudio and Wasowski 2007), D (Directional)-SSR (Standard spectral ratio) (Gaudio and Wasowski 2007) and D (Directional)-SER (Seismic energy ratio).

D-Arias was used to detect the anisotropic Arias intensity and the conventional Arias intensity with zero damping as calculated by (Arias 1970, 1996):

$$I_{ij} = \frac{\pi}{2g} \int_{t_i}^{t_f} a_i(t) \times a_j(t) dt \quad i, j = 1, 2, 3 \quad (1)$$

where g is gravitational acceleration, $a(t)$ is acceleration, and the indexes i and j are components of a . t_i and t_f are the initial and final local ground shaking times caused by a seismic event, respectively. Several studies have noted the strongest dynamic responses mainly arise from horizontal shaking (Kubo and Penzien 1979; Katayama 1991; Gaudio and Wasowski 2007; Gaudio et al. 2015). Additionally, the Arias intensity along a horizontal direction is obtained by (Gaudio et al. 2014):

$$I_{\alpha} = I_e \times \sin^2(\alpha) + I_n \times \cos^2(\alpha) + I_{en} \times \sin(2\alpha) \quad (2)$$

where I_e and I_n are the east and west Arias intensities, respectively, and I_{en} is the result of integrating the east and north components of acceleration. The maximum and minimum shaking

amounts are obtained when the derivative of Eq.2 equals 0. The second derivative of Eq.2 produces two oppositely directed maxima, $I_{\alpha M}$, which are orthogonal to the two opposite minima, $I_{\alpha m}$ (Gaudio et al. 2014). Thus, by substituting the angles in Eq. 2, the values of $I_{\alpha m}$ and $I_{\alpha M}$ can be determined. Their ratio provides a parameter that represents an isotropy index that ranges between the two asymptotic limits of 0 and 1; these limits represent the ideal cases of perfectly linearly polarized shaking or perfectly isotropic shaking, respectively (0- linearly polarized shaking and 1- isotropic shaking, Gaudio et al. 2014).

D-SSR is the polarized standard spectral ratio; the reference accelerograph for the LZG station is L7-5 (L7R), as listed in Table 1, which is located in the interior of the mountain; the polarization method is discussed in Gaudio and Wasowski (2007). D-HVSr is the polarized horizontal-to-vertical spectral ratio and is commonly used to detect the resonance properties of sites (Nakamura 1989); the polarization method is discussed in Gaudio and Wasowski (2007).

D-SER is calculated from the shaking energy ratio between two accelerographs at every azimuth for horizontal shaking. The calculation process was as follows: first examine the shaking recordings at every azimuth (bin = 10°) for horizontal shaking, then calculate their shaking energies, and finally, calculate the ratios for every azimuth between the two accelerographs; the reference accelerograph was L7R.

3 Results

3.1 Sites L1-L2

Figure 5 shows polar diagrams for the D-Arias and D-HVSr data from the Lushan and Kangding

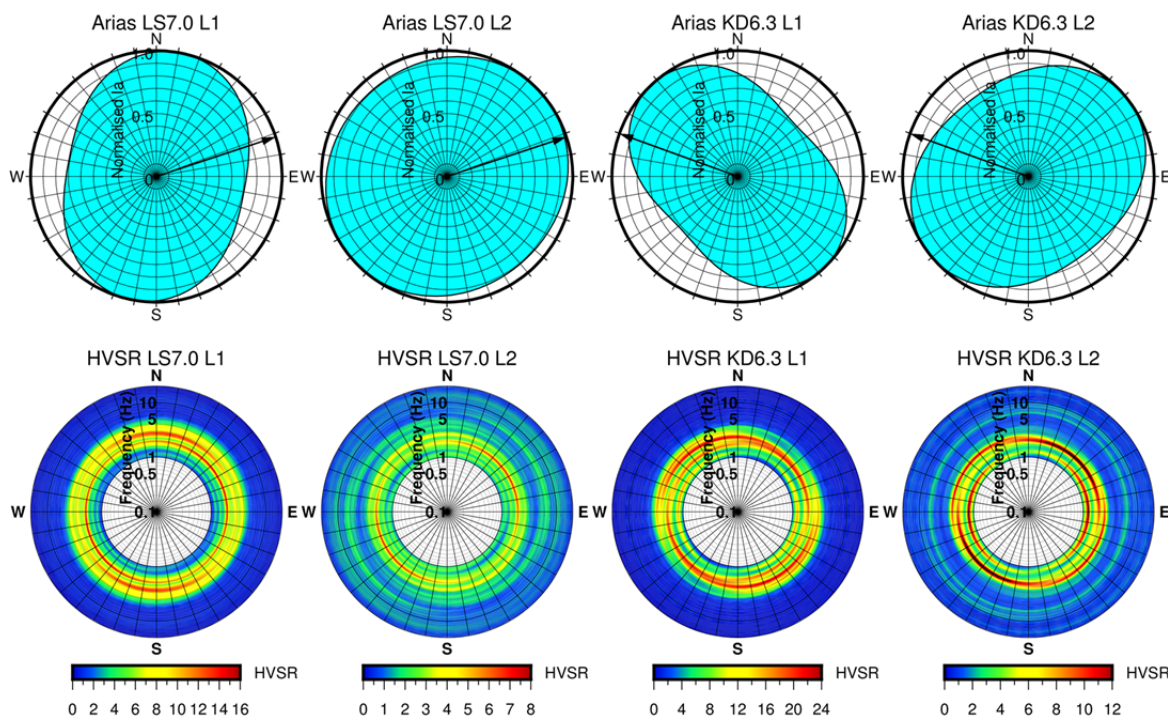


Figure 5 The polar diagrams of D-Arial (Directional - Arias) and D-HVSR (Directional - Horizontal to vertical spectral ratio) of Sites L1 and L2.

events. From Figure 5, the Arias intensity for L1, which was located on the ridge top, presents a more obvious anisotropic distribution than that for site L2, which was located on the middle part of the ridge. For the Lushan event, the antistrophic index I_{ra} of L1 was 0.707, whose pronounced response direction was approximately N21°E; the I_{ra} value for L2 reached 0.907, whose pronounced response direction was oriented approximately N48°E (Figure 5). For the Kangding event, the antistrophic index I_{ra} for L1 was 0.614, whose pronounced response direction was oriented approximately N45°W; the I_{ra} value for L2 reached 0.758, whose pronounced response direction was oriented approximately N53°E (Figure 5).

The HVSR results for the two seismic events were similar (Figures 5 and 6). The HVSR distributions of the two events both indicated consistent evidence for site resonance of L1 and L2 between frequencies of 2 and 5 Hz, especially near 2 Hz (Figures 5 and 6). The HVSR results for L1 presented a sharper distribution at 2-3 Hz (Figure 6). The overall directional site resonance for L1 and L2 indicated an obvious site response for the ridge body, especially for L1 (ridge top), as shown in Figure 5. In addition, the nearly SE direction of the two accelerographs both recorded the strongest site

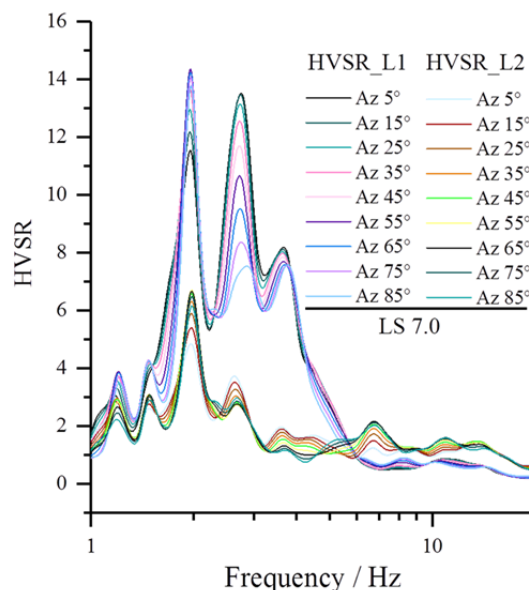


Figure 6 The comparison curves of HVSR (Horizontal to vertical spectral ratios) of different Az (azimuths) (0°-90°) for site L1 and L2 (Lushan earthquake).

resonance.

As illustrated in Figure 6, the site resonance intensity (HVSR value) induced by the Kangding event was stronger than that induced by the Lushan event despite the fact that the Lushan event had a higher magnitude. Actually, obvious attenuation

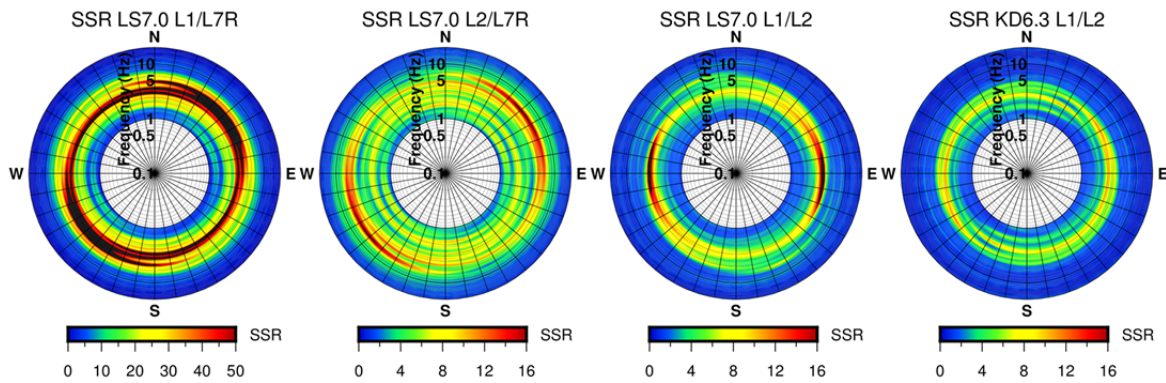


Figure 7 The polar diagrams of D-SSR (Directional - Standard spectral ratio) of Sites L1 and L2.

occurs in the process of seismic wave propagation, especially for long-distance propagation in surface-fractured mountains (Nuttli 1973; Liu et al 2004), which means that the shorter the distance, the higher the intensity. The LZG station is approximately 51 km from the KD event, which is only 59% of the distance from the LZG station to the LS event (81 km). Therefore, the KD events with shorter distances caused stronger site resonances.

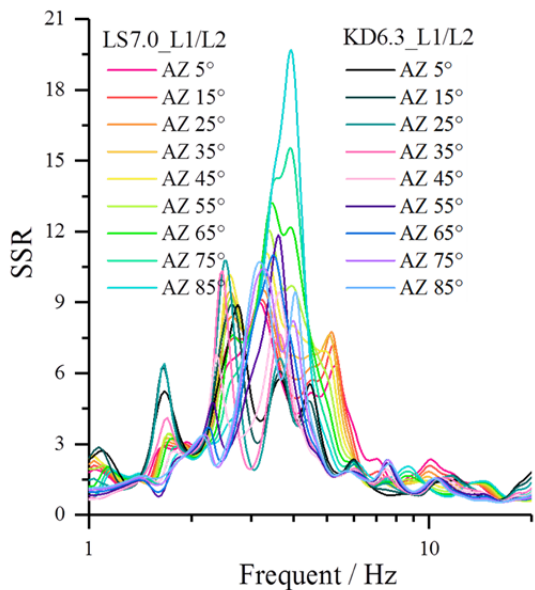


Figure 8 The comparison curves of SSR (Standard spectral ratio) of different Az (azimuths) (0° - 90°) for site L1 and L2.

As indicated in Section 1.3, site L7-5, which was located inside the mountain, served as the reference accelerograph (L7R); the D-SSR data from L1 and L2 for the two events are shown in Figure 7. Compared to L7R, the L1 and L2 data both indicate overall site amplification (Figures 7 and 8), especially for L1, whose amplification value

reached a striking value of 90 (Figure 8), whereas the peak value for L2 reached approximately 16. The SSR results of L1 to L2 that were induced by the two seismic events were similar, and both showed that the ridge top produced a more obvious amplification than the lower areas, whose amplitudes reached 20 and 12, respectively (Figure 8). The site resonant frequency, as indicated by the four SSRs, was concentrated from 2-8 Hz and was focused between 2 and 5 Hz, which agrees with the pronounced site frequency revealed by HVSR.

The D-SER values also indicated similar pronounced site amplification levels compared with SSR (Figure 9): the L1 and L2 sites both exhibited obvious site amplification compared to L7R, especially for L1, whose peak energy ratio reached into the hundreds, while the peak energy ratio for L2 reached 16. The pronounced site amplifications for the two sites were consistent, especially in the E-SE direction.

The SERs from L1 and L2 that were induced by the two seismic events show that the ridge top produced stronger shaking than the lower part, whose SER reached into the hundreds, while their pronounced response directions were slightly different.

The Figure 10 shows the pronounced response direction distributions of L1 and L2 that were induced by the two seismic events. The two seismic events with different distances to the LZG station (e.g., Lushan event: 86 km and Kangding event: 51 km) and different azimuths of seismic wave propagation (Lushan event: 287.4° and Kangding event: 117.6°) caused similar (HVSR and SSR) pronounced site frequencies of 2 to 5 Hz and pronounced response directions from $N30^{\circ}$ $70^{\circ}E$ with only slight differences in shaking energy

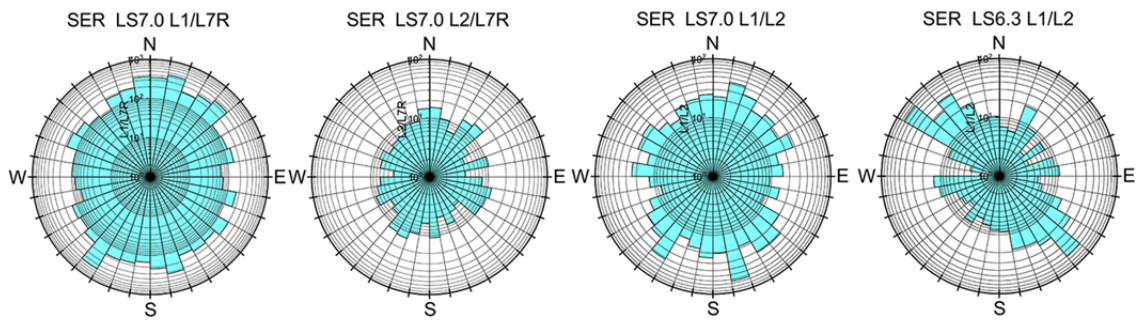


Figure 9 The polar diagrams of D-SER (Shaking energy ratios) of sites L1 and L2.

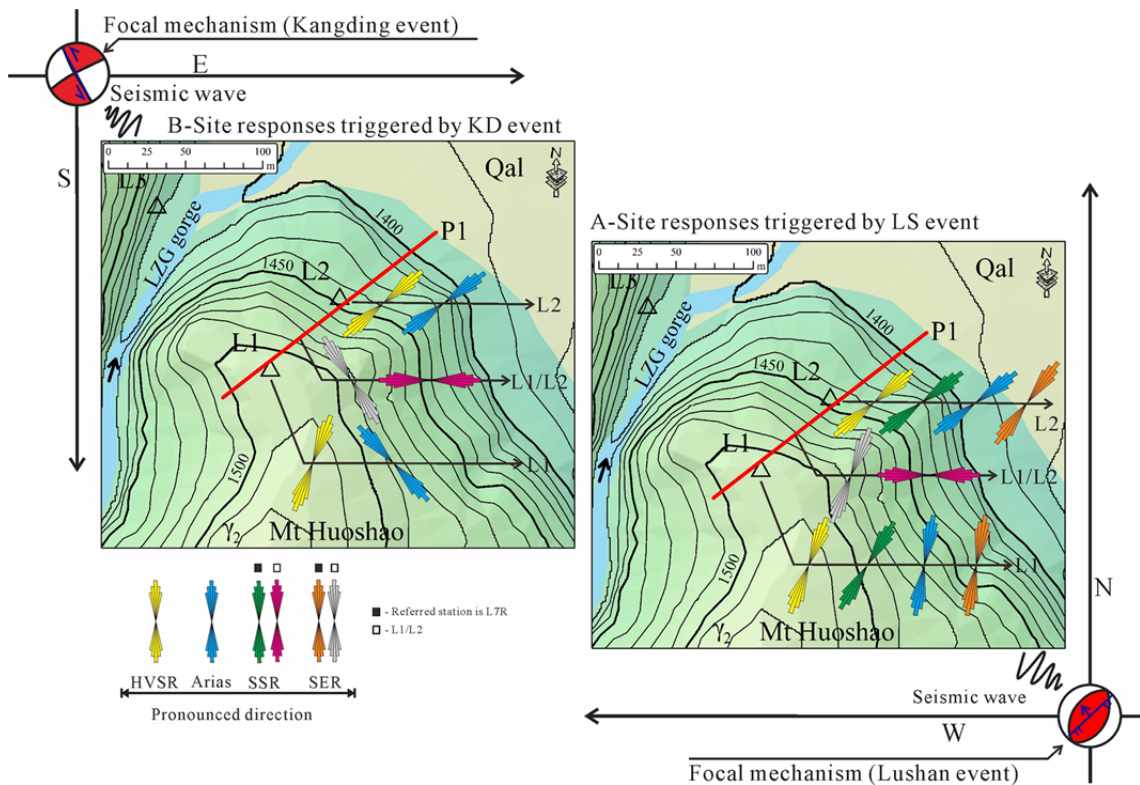


Figure 10 The pronounced response direction distribution of L1 and L2 triggered by Lushan earthquake (A) and Kangding earthquake (B).

(Arias and SER). The Arias and SER values at L2 (middle part of the isolated ridge) for different events generated similar pronounced response directions (Figures 6, 10 and 11), while the Arias and SER values for L1 (top part of the isolated ridge) changed along with the event locations and roughly coincided with the propagation directions of the seismic waves.

3.2 Sites L4 and L5

Sites L4 and L5 are located at a transition zone and slope break section on the left side of the

Lengzhuguan Valley, respectively (Figures 3, 4). Figure 11 shows the polar diagrams for D-Arias, D-HVSR, D-SSR and D-SER for L4. From Figure 11, different polarization methods presented similar pronounced response directions, e.g., near N 20°-30°E. The Arias distribution presented a “peanut” shape, and the I_{ra} value for L4 reached 0.604, while the pronounced response direction was approximately N20°-30°E.

The site resonant frequencies, as indicated by HVSR, were mainly between 11 and 15 Hz with pear-shaped values that reached 3.4 (Figures 11). There were three obvious peak waveforms at 4-5

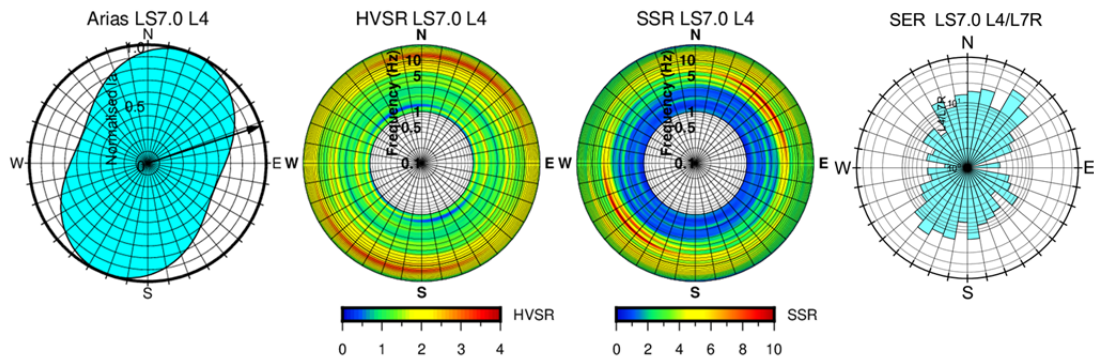


Figure 11 The polar diagrams of D-Arias (Directional- Arias), D-HVSR (Directional – Horizontal to vertical spectral ratio), D-SSR (Directional – Standard spectral ratio) and D-SER (Directional - Shaking energy ratio) of sites L4.

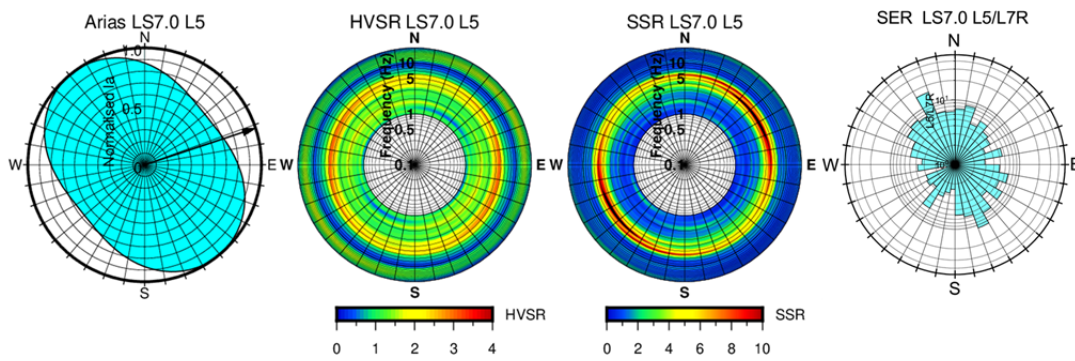


Figure 13 The polar diagrams of D-Arias (Directional- Arias), D-HVSR (Directional – Horizontal to vertical spectral ratio), D-SSR (Directional – Standard spectral ratio) and D-SER (Directional - Shaking energy ratios) of site L5.

Hz, 5-6 Hz and 11-13 Hz (Figure 12). The HVSR and SSR data showed good consistency between 11 and 13 Hz (Figure 12). The SER data indicated obvious site amplification at N40°-50°E, and the peak value reached 11.5.

Sites L2 and L4 are located at similar elevations and are under similar geological conditions but are on different riverbanks (the left bank is a very large mountain, while the right bank is an isolated ridge, as is listed in Table 2); the site response of L2 was clearly much stronger than that of L4, which may indicate that the isolated ridge is more sensitive to seismic shaking than the large mountain.

Figure 13 shows the polar diagrams of the D-Arias, D-HVSR, D-SSR and D-SER data from L5. From Figure 13, the four polarization diagrams all show pronounced site responses at azimuths near N30°-50°W. The Arias distribution also showed a “peanut” shape, and the $I_{r\alpha}$ values for L5 reached 0.673, while the pronounced site response was oriented at approximately N38°W. The site resonant frequency, as indicated by HVSR, was within 2.5-4.5 Hz with a pear shape that reached 3.6 (Figures 13). There was obvious site

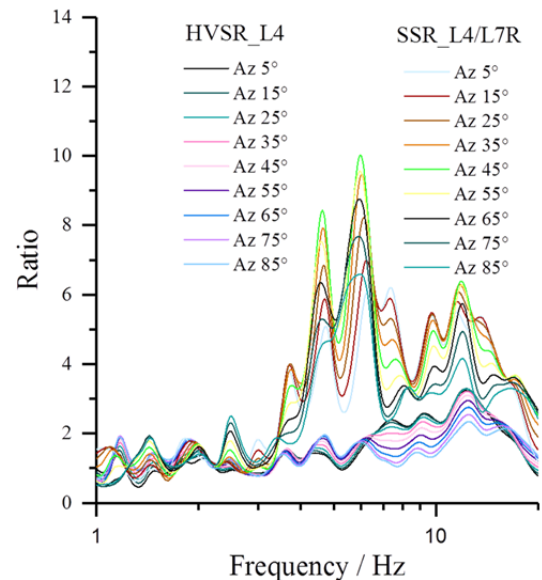


Figure 12 The comparison curves of HVSR (Horizontal to vertical spectral ratio) and SSR (Standard spectral ratio) of different Az (azimuths) (0°-90°) for site L4. amplification at 3.5-6.5 Hz, whose peak value reached 12, as indicated by SSR (Figure 14). The HVSR and SSR data showed good consistency at 3.5-4.5 Hz (Figure 14) and showed overall site

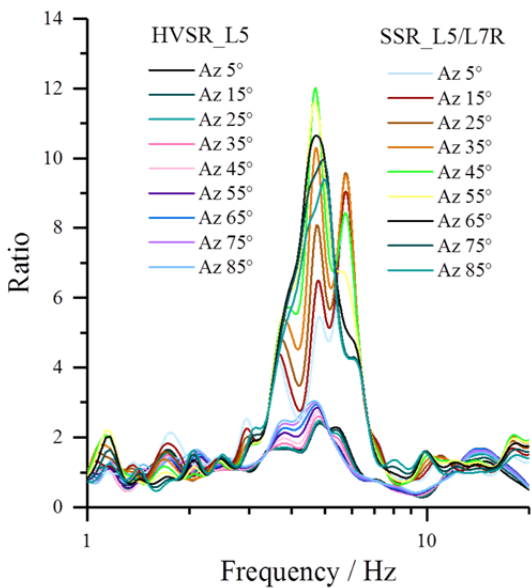


Figure 14 The comparison curves of HVSR (Horizontal to vertical spectral ratio) and SSR (Standard spectral ratio) of different Az (azimuths) (0°-90°) for site L5.

amplification at N40°-60°E. The SER data showed obvious site amplification at N40°-50°E, and the peak value reached 10.8 (Figure 13).

L4 and L5, which are both in a steep zone in the vertical and horizontal directions, are located in the lower part (m.a.s.l 1494 m) and higher part (m.a.s.l 1518 m), respectively. Different from the change rules for the responses of sites L1 and L2 (greater relief and stronger site response), the lower site (site L4) exhibited similar site amplifications under similar geological conditions compared with L5 (Figure 15). The pronounced response directions of L4 and L5 were oriented near N40°-60°E and N30°-50°W, respectively, for the same propagation direction of seismic wave (Figure 15).

3.3 Sites L6-L7

Site L6 is located on a nearby rectilinear slope, and the four polarization diagrams both showed pronounced site responses at an azimuth near N60°-80°E (Figure 16). The Arias distribution presented a fat “peanut” shape, and the I_{ra} value for L6 reached 0.795, while the pronounced site response is oriented approximately N70°W. The site resonance of L6 was very weak, and the peak

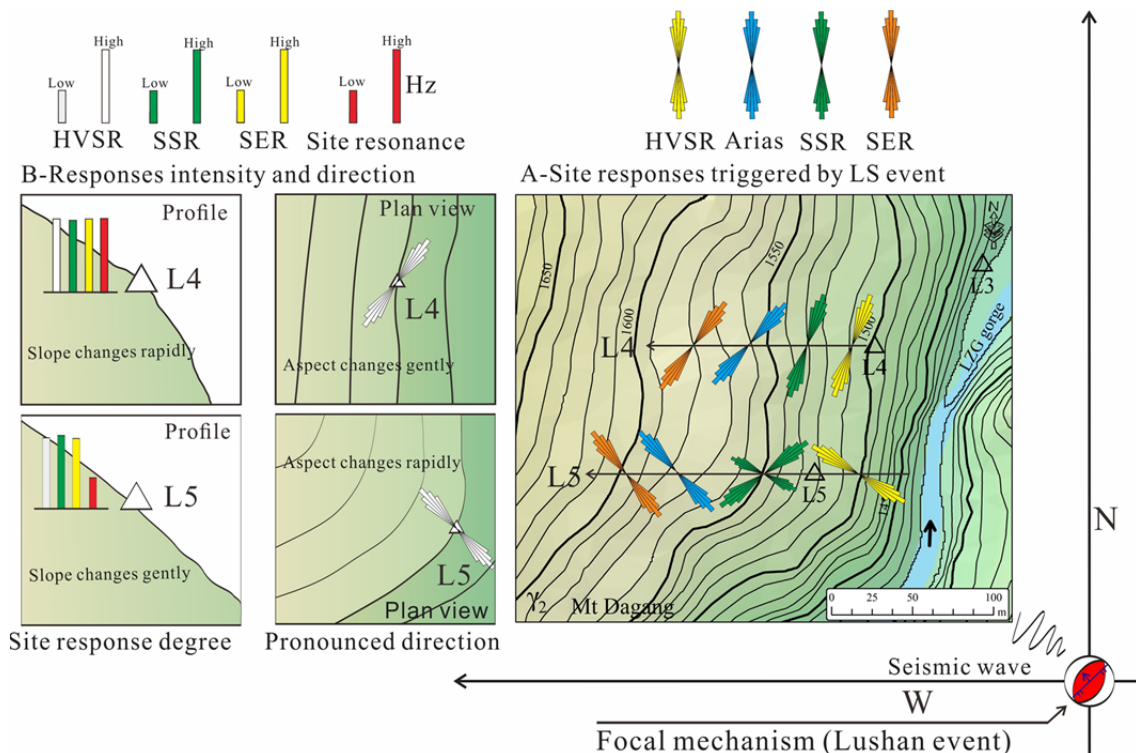


Figure 15 The pronounced response direction and response intensity of L4 and L5 triggered by Lushan earthquake. A - Pronounced response direction result calculated by different methods, B - The response intensity and comprehensive pronounced response direction. The L4 is located in the transition zone between gentle slope (upper section < 30°) and steep slope (lower section > 50°) while gentle changes in aspect. The L5 is located in slope break section whose aspect changes rapidly while gentle changes in slope.

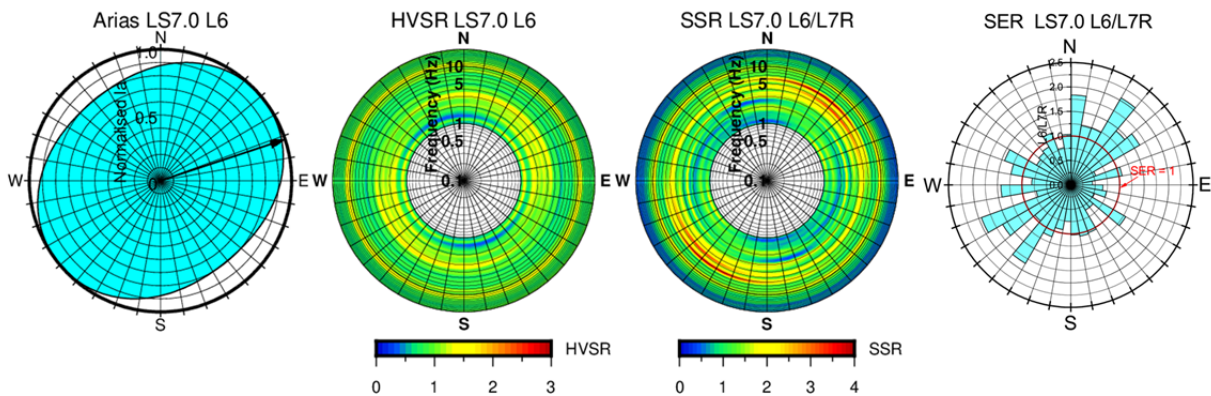


Figure 16 The polar diagrams of D-Arias (Directional- Arias), D-HVSR (Directional – Horizontal to vertical spectral ratio), D-SSR (Directional – Standard spectral ratio) and D-SER (Directional - Shaking energy ratio) of site L6.

value was only approximately 1.8 (< 2.0) near 3.0 Hz (azimuth: $N60^{\circ}$ - $75^{\circ}E$), as shown in Figures 16 and 17. The SSR data showed multi-peak waveforms at 2-6 Hz with a peak value at approximately 3.6 Hz, which was oriented at $N45$ - $70^{\circ}E$ (Figures 16, 17), and both showed relatively stronger site responses at 3 Hz, as was indicated by the HVSR and SSR data. The SER data also showed NE site amplification with a peak value of approximately 2.0 (Figure 17).

There are two active accelerographs at site L7 (e.g., L7-1 and L7R); L7-1 and L7R are located 50 m and 250 m from the slope surface, respectively (Figure 4E). Figure 18 shows the polar diagrams of the D-Arias, D-HVSR, D-SSR and D-SER data from L7-1 and the D-Arias and D-HVSR data from L7R

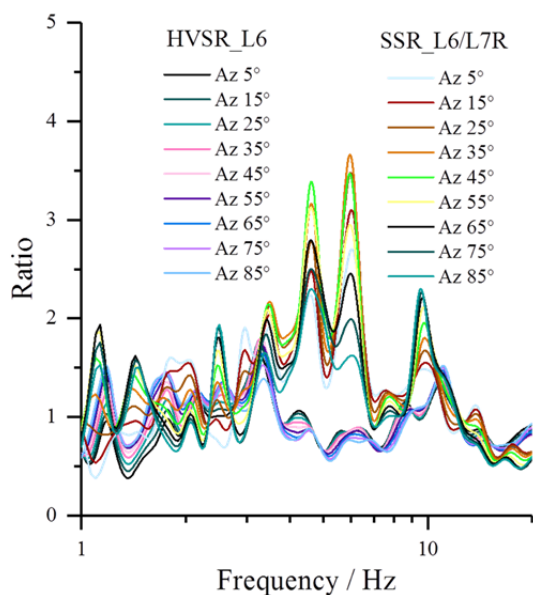


Figure 17 The comparison curves of HVSR (Horizontal to vertical spectral ratio) and SSR (Standard spectral ratio) of different Az (azimuths) (0° - 90°) for site L6.

(L7-5). From Figure 18, the four polarization diagrams all showed pronounced site responses at

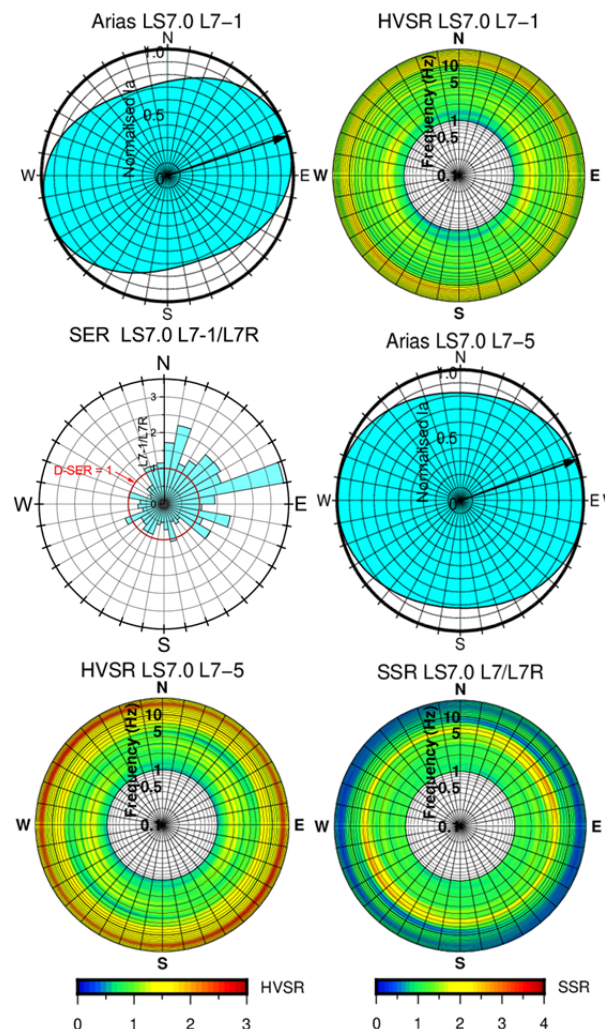


Figure 18 The polar diagrams of D-Arias (Directional- Arias), D-HVSR (Directional – Horizontal to vertical spectral ratio), D-SSR (Directional – Standard spectral ratio) and D-SER (Directional - Shaking energy ratios) of Sites L7-1 and L7R.

azimuths near NE-NEE. The Arias distribution also showed a fat “peanut” shape, and the I_{ra} value of L6 reached 0.719 with a pronounced site response oriented approximately N70°-90°E. The site resonance for site L7-1 was also very weak, with a peak value of only approximately 1.9 (< 2.0) near 11-13 Hz; the SSR data showed a peak value of 2.6 at frequencies of 4-6 Hz; the SER data showed a peak value of 3.8 at an azimuth of N70°-90°E (Figure 18).

L7R (L7-5) is the reference site, and the Arias distribution presented an elliptical shape with an I_{ra} value for L7 of 0.824; there was a relative peak waveform (HVSr) at 15-17 Hz with a peak value of approximately 2.4, and there was no clear pronounced site resonance azimuth (Figure 18).

For sites L7-1 and L7R, which were at located different depths within the mountain body, the site resonant frequency for the outer site (L7-1: 11-13 Hz) was somewhat smaller than that for the inner site (L7R: 15-17 Hz), as shown in Figures 18 and 19.

As shown in Figure 19, the pronounced response directions inside the mountain (L7 and L7R) both followed an EW direction, which was

Table 3 The PGA (peak ground acceleration) ratios of all activated sites, the reference site is L7R

Accelerograph	PGA Ratio			Elevation (m)
	NS	EW	UD	
L1/L7R	11.06	12.97	6.01	1516
L2/L7R	2.83	3.37	2.61	1478
L4/L7R	2.22	2.90	1.83	1494
L5/L7R	1.57	2.40	2.25	1518
L6/L7R	1.05	0.89	1.40	1520
L7-1/L7R	1.33	0.87	1.14	1686
L7R/L7R	1	1	1	1686

perpendicular to the direction of mountain extension; the L6 direction was oriented at N70°-80°E, which was roughly parallel to the slope aspect. In addition, the response intensity of L7-1 was slightly stronger than that of L6 despite the fact that L7-1 is located slightly inside the mountain (Depth: 50 m).

4 Discussion

Based on the seismic data and relevant analyses, the PGA ratios for all the active sites,

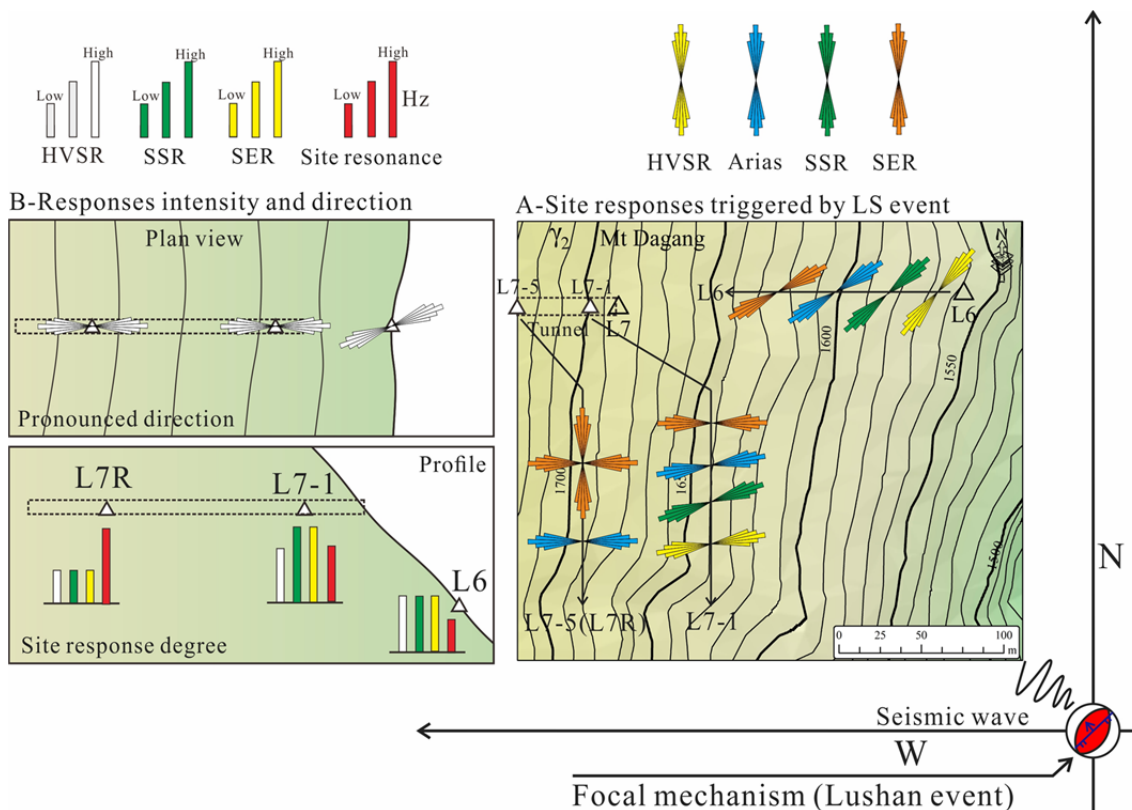


Figure 19 The pronounced response direction and response intensity of L6 and L7 triggered by Lushan earthquake. A - Pronounced response direction result calculated by different methods, B - The response intensity and comprehensive pronounced response direction.

dynamic response intensities and pronounced directions that were induced by the Lushan event are shown in Table 3 and Figure 20, respectively. The Lushan event was a thrust earthquake, and its epicentre was approximately 86 km from the LZG station at a bearing of N72.6°E from the LZG station. The propagation direction of the seismic waves was approximately 287.4°.

As shown in Table 3 and Figure 20, the one

seismic event with the same seismic wave propagation direction did not cause the same or similar site response at L1-L7R, and the truth is that different sites present clearly different responses.

(1) The isolated ridge (narrow hill) can cause stronger dynamic responses than the large mountain (fat hill) with a similar relief when comparing L1 and L2 (the isolated ridge) with L4,

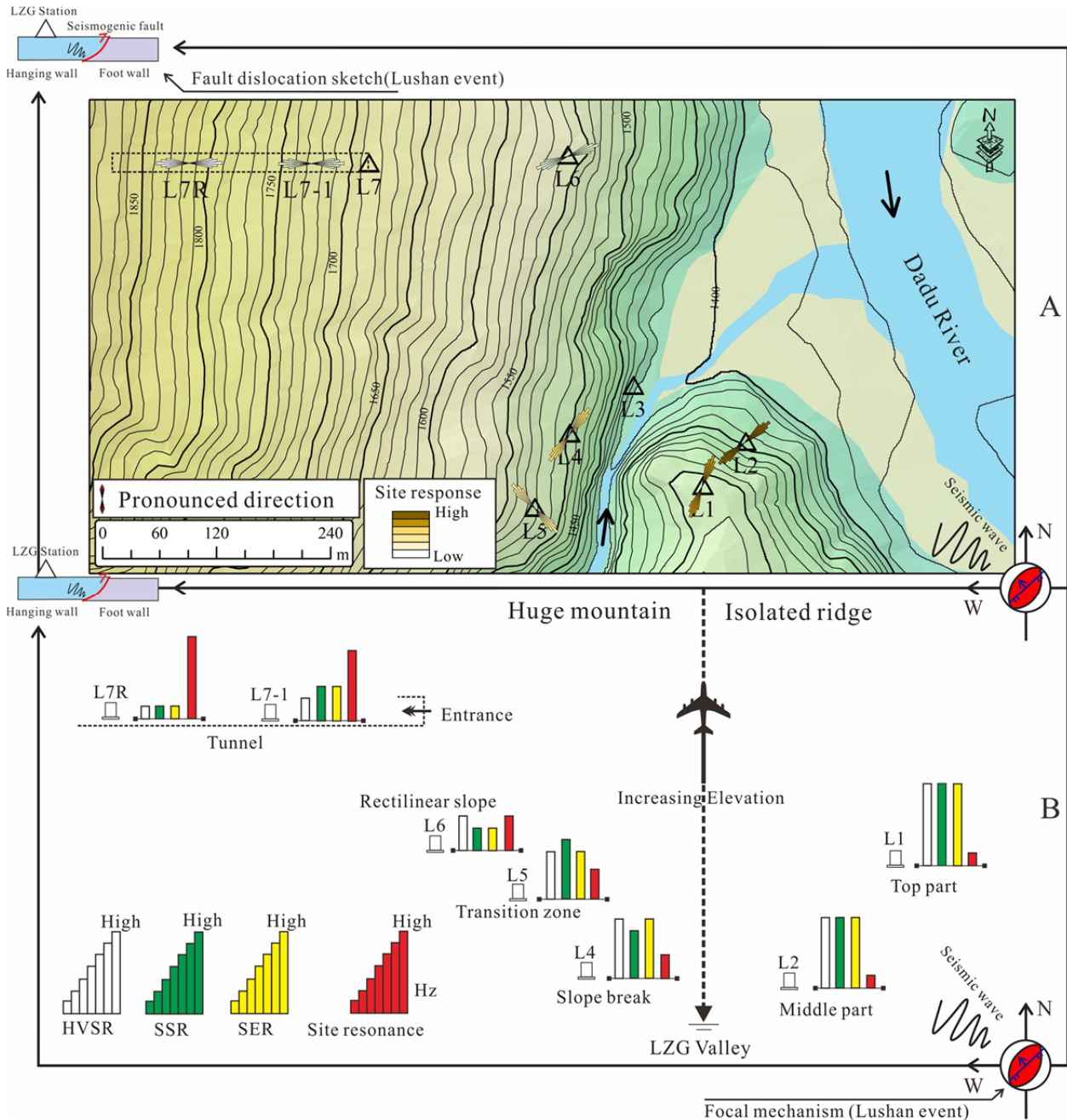


Figure 20 The pronounced response direction of all sites triggered by Lushan earthquake, the site response degree of different sites triggered Lushan earthquake.

L5 and L6 (the large mountain). This finding indicates that under similar seismic shaking levels, the narrow hill could generally cause geohazards that were more serious than those caused by the fat hill. This phenomenon was common in the Wenchuan earthquake, Lushan earthquake and Jiuzhaigou earthquake (Luo et al. 2014; Huang et al. 2011; Hu et al. 2013; Zhao et al. 2018).

(2) For the isolated ridge, with increased elevation, the dynamic response became stronger with no obvious variation in the resonant frequency (2-5 Hz); the pronounced response directions for L1 and L2 were similar and were nearly perpendicular to the ridge trend (L1) and slope (L2). The intense site amplification caused the top section of the isolated ridge to be a large-scale landslide-prone area; many large-scale landslides were triggered by the Wenchuan earthquake, such as the Donghekou landslide, Wenjiagou landslide, Dayanqiao landslide, and Niumiangou landslide and all occurred in this section (Xu et al. 2009b). Actually, geohazards in general are more likely to occur in this section (Zhao et al. 2019, 2020).

(3) L4, L5 and L6 are located on the large mountain with different micro-relief and elevations. For these 3 sites, with increased elevation, the resonant frequency decreased while the different micro-relief features exhibited different site responses than the slope break and transition zone; with both belonging to protruding slope, this could cause stronger site responses than rectilinear slopes; the pronounced response directions were also influenced differently by the micro-relief features (Figure 20).

(4) L7-1 and L7R were inside the mountain body, and their site responses were significantly weaker than those of the other sites despite their higher elevations (Table 3, Figure 20). The site response of the outer site (L7-1) was relatively stronger than that of the inner site (L7R), which was located deeper in the mountain and had a weaker site response and higher site resonant frequency (Figures 16, 17). The pronounced response directions of the two sites were similar and were nearly perpendicular to the ridge trend, especially for the inner site (Figure 20). Site L7R is most suitable as a reference site due to its weakest site response. The surface site response indicated that surface slopes are seismic landslide-prone areas,

which agrees with field investigations that showed that more than 90% of the landslides that were triggered by the Wenchuan earthquake were surface landslides whose depths ranged from several meters to approximately ten meters (Huang et al. 2009). Similar phenomena also appear for the Lushan earthquake, Jiuzhaigou earthquake and Nyingchi earthquake (Tang et al. 2015; Zhao et al. 2018; Fan et al. 2018; Zhao et al. 2019).

(5) Comparison with other studies. Gaudio and Wasowski (2007), Gaudio et al. (2014), Luo et al. (2014) also conducted similar site response directivity analyses in the Caramanico area of Italy, Iranian area and Qingchuan area of Sichuan Province in China, respectively. The Caramanico station is in a hilly area with relief ranging from 50 m to 250 m, and its lithology consists of limestone and mudstone, which indicates that every accelerograph site can present a pronounced response direction and will usually be influenced by slope material properties (Gaudio and Wasowski 2007). Five scattered accelerograph sites in the Iranian area were adopted to calculate their pronounced response directions and measure the pronounced systematic anisotropy of ground shaking that was not dependent on source characteristics but rather on structural elements (e.g., faults and folds) (Gaudio et al. 2014). The Qingchuan station is located on hills in a peri-urban zone and measures the opposite relationships between resonant frequencies and hill size; the local geology also plays a significant role in differentiating the site responses (Luo et al. 2014). Actually, all of these studies focused on small earthquakes (e.g., maximum magnitude: Ms 5.5) and hilly areas; the directional site responses to large earthquakes and complex geomorphic units deserve deeper investigation. The eastern margin of the Tibetan Plateau is famous for its widespread tectonic and seismic activity, and the deep-cutting gorge and seismic geohazards at this margin are mainly triggered by large earthquakes (magnitude ≥ 6.0 , Xu et al. 2009b; Huang et al. 2009; Xu et al. 2014; Tang et al. 2015; Cao et al. 2015; Zhao et al. 2018, 2019). This study used seismic data from two large earthquakes to analyse the directional seismic responses to the deep-cutting gorge and local geomorphic units at the eastern margin of the Tibetan Plateau; the results of this study can provide guidance for detecting

seismic landslide-prone areas that are influenced by different geomorphic units.

5 Conclusions

Four polarization methods (e.g., D-Arias, D-HVSR, D-SSR and D-SER) are adopted to process seismic data from the Lushan Ms 7.0 earthquake as captured by the Lengzhuguan station, which is located upstream of the Dadu River with typical topographic features. The outcomes offer insights into the characteristics of the azimuthal variations of seismic responses to sites with different topographies, elevations and mountains.

The isolated ridge usually caused stronger site responses than the large mountain, which also had lower site resonant frequencies (2-5 Hz); the pronounced response directions were nearly perpendicular to the ridgeline and, with increasing elevation, the site responses became stronger. Different seismic events showed little influence on the resonant frequencies of the site and the corresponding response directions, while the shaking energy at the top part of the isolated ridge changed with the locations of the seismic events and roughly coincided with the propagation directions of the seismic waves.

For the large mountain, with increased

elevations, the site resonant frequency decreased, and local relief had an important influence on the site responses, with protruding slope (slope break, transition zone) > rectilinear slope.

Areas outside the mountain body caused stronger site responses than those inside the mountain body, which indicates that the deeper inside a mountain, the weaker responses, the higher the resonant frequencies, and more stable the pronounced response directions (i.e., perpendicular to the ridgeline).

Acknowledgement

This study was supported by the National Natural Science Foundation of China (Grant No. 41877235), the National Key Research and Development Program of China (Grant No. 2017YFC1501000), China Postdoctoral Science Foundation (2020M673292), and the National Science Funds for Creative Research Groups of China (Grant No. 41521002). The authors are sincerely thankful to Prof. Vincenzo Del Gaudio for providing polarization method and useful discussions, to Prof. Janusz Wasowski for discussing the field conditions of Lengzhuguan Station, and to Dr. HE Jianxian for seismic data recording.

References

- Arias A (1970) A measure of earthquake intensity, in *Seismic Design for Nuclear Power Plants* (ed. Hansen R.J). MIT Press, Cambridge, Massachusetts. pp 438-483.
- Arias A (1996) Local directivity of strong ground motion. In *Proc. Eleventh World Conference on Earthquake Engineering*, Elsevier Science Ltd, ISBN:0-08-042822-2, pp. 1-8.
- Ashford SA, Sitar N (1997) Analysis of Topographic Amplification of Inclined Shear Waves in a Steep Coastal Bluff. *Bulletin of the Seismological Society of America* 87(3):692-700
- Borcherdt RD (1970) Effects of local geology on ground motion near San Francisco Bay. *Bulletin of the Seismological Society of America* 60(1): 29-61.
- Bourdeau C, Havenith HB (2008) Site effects modelling applied to the slope affected by the suusamy earthquake (Kyrgyzstan, 1992). *Engineering Geology* 97(3-4):126-145. <https://doi.org/10.1016/j.enggeo.2007.12.009>
- Cao SH, Wang YS, He JX (2015) Characteristics and disaster model of co-seismic landslides triggered by the Kangding Ms 6.3 earthquake on the 22th of November, Sichuan province, China. *The Chinese Journal of Geological Hazard and Control* 26(4): 87-93. (In Chinese) <https://doi:16031/k.cnki.issn.1003-8035.2015.04.15>
- Dai F, Lee C, Deng J, Tham L (2005) The 1786 earthquake-triggered landslide dam and subsequent dam-break flood on the Dadu River, southwestern China. *Geomorphology* 73(3): 277-278. <https://doi.org/10.1016/j.geomorph.2005.06.011>
- Deng H, Wu LZ, Huang RQ, et al. (2017) Formation of the Siwanli ancient landslide in the Dadu River, China. *Landslides* 14(1): 385-394. <https://doi.org/10.1007/s10346-016-0756-9>
- Fan X, Scaringi G, Xu Q, et al. (2018) Coseismic landslides triggered by the 8th August 2017 Ms 7.0 Jiuzhaigou earthquake (Sichuan, China): factors controlling their spatial distribution and implications for the seismogenic blind fault identification. *Landslides* 15(5):967-983. <https://doi.org/10.1007/s10346-018-0960-x>
- Fan X, Westen CJV, Xu Q, et al. (2012) Analysis of landslide dams induced by the 2008 Wenchuan earthquake. *Journal of Asian Earth Sciences* 57: 25-37. <https://doi.org/10.1016/j.jseaes.2012.06.002>
- Fiore VD (2010) Seismic site amplification induced by topographic irregularity: results of a numerical analysis on 2d synthetic models. *Engineering Geology* 114(3-4): 109-115. <https://doi.org/10.1016/j.enggeo.2010.05.006>
- Gaudio VD, Coccia S, Wasowski J, et al. (2008) Detection of directivity in seismic site response from microtremor spectral analysis. *Natural Hazards and Earth System Sciences* 8(4): 751-762. <https://doi.org/10.5194/nhess-8-751-2008>
- Gaudio VD, Muscillo S, Wasowski J (2014) What we can learn

- about slope response to earthquakes from ambient noise analysis: an overview. *Engineering Geology* 182: 182-200. <https://doi.org/10.1016/j.enggeo.2014.05.010>
- Gaudio VD, Pierri P, Rajabi AM (2015) An approach to identify site response directivity of accelerometer sites and application to the Iranian area. *Pure and Applied Geophysics* 172(6): 1471-1490. <https://doi.org/10.1007/s00024-014-1003-8>
- Gaudio VD, Wasowski J (2007) Directivity of slope dynamic response to seismic shaking. *Geophysical Research Letters* 34(12): 107-124. <https://doi.org/10.1029/2007GL029842>
- Gaudio VD, Wasowski J (2011) Advances and problems in understanding the seismic response of potentially unstable slopes. *Engineering Geology* 122(1): 73-83. <https://doi.org/10.1016/j.enggeo.2010.09.007>
- Geli L, Bard PY, Jullien B (1988) The effect of topography on earthquake ground motion: A review and new results. *Bulletin of the Seismological Society of America* 78(1):42-63.
- Gorum T, Fan X, Van Westen CJ, et al. (2011) Distribution pattern of earthquake-induced landslides triggered by the 12 May 2008 Wenchuan earthquake. *Geomorphology* 133(3-4): 152-167. <https://doi.org/10.1016/j.geomorph.2010.12.030>
- Harp EL, Jibson RW (2002) Anomalous concentrations of seismically triggered rock falls in Pacoima Canyon: are they caused by highly susceptible slopes or local amplification of seismic shaking? *Bulletin of the Seismological Society of America* 92: 3180-3189. <https://doi.org/10.1785/0120010171>
- Hu X, Lin J, Zhang M, et al. (2013) Trigger effect of earthquake geohazards around baoxing county induced by lushan 4-20 strong earthquake. *Journal of Southwest Jiaotong University* 48(4): 599-608. (In Chinese) <https://doi.org/10.3969/j.issn.0258-2724.2013.04.003>
- Huang R (2009) Geohazard assessment of the Wenchuan earthquake. Science Press, Beijing. (In Chinese)
- Huang R, Xu Q, Huo J (2011) Mechanism and geo-mechanics models of landslides triggered by 5.12 Wenchuan earthquake. *Journal of Mountain Science* 8(2): 200-210. <https://doi.org/10.1007/s11629-011-2104-9>
- Katayama T, Yamazaki F, Nagata S, et al. (1990) A strong motion database for the Chiba seismometer array and its engineering analysis. *Earthquake Engineering and Structural Dynamics* 19(8): 1089-1106. <https://doi.org/10.1002/eqe.4290190802>
- Kubo T, Penzien J (1979) Analysis of three - dimensional strong ground motions along principal axes, San Fernando earthquake. *Earthquake Engineering and Structural Dynamics* 7(3): 265-278. <https://doi.org/10.1002/eqe.4290070306>
- Lermo J, Chávez-García FJ (1993) Site effect evaluation using spectral ratios with only one station. *Bulletin of the seismological society of America* 83(5): 1574-1594.
- Li YS, Wang YS, Pei XJ (2013) Research on tectonic fracturing and causative fault of Lushan earthquake in Sichuan, China. *Journal of Chengdu University of Technology* 40(3): 242-249. (In Chinese) <https://doi.org/10.3969/j.issn.1671-9727.2013.03.03>
- Liu JH, Xu Y, Hao TY (2004) Study on physical mechanism of the seismic wave attenuation. *Progress In Geophysics* 19(1): 1-7. (In Chinese)
- Liu CL, Zheng Y, Ge C, et al. (2013) Rupture process of the M7.0 Lushan earthquake. *Science China* 56(7): 1187-1192. <https://doi.org/10.1360/zd-2013-43-6-1020>
- Luo YH, Gaudio VD, Huang R, et al. (2014) Evidence of hillslope directional amplification from accelerometer recordings at Qiaozhuang (Sichuan - China). *Engineering Geology* 183:193-207. <https://doi.org/10.1016/j.enggeo.2014.10.015>
- Luo YH, Wang YS, He Y (2013) Monitoring result analysis of Lengzhuguan slope ground shock response of Lushan earthquake of Sichuan, China. *Journal of Chengdu University of Technology* 40(3):232-241. (In Chinese with English Abstract). <https://doi.org/10.3969/j.issn.1671-9727.2013.03.02>
- Nakamura Y (1989) A method for dynamic characteristics estimation of subsurface using microtremor on the ground surface. *Railway Technical Research Institute, Quarterly Reports* 30(1): 25-33.
- Nuttli OW (1973) Seismic wave attenuation and magnitude relations for eastern North America. *Journal of Geophysical Research* 78(5): 876-885. <https://doi.org/10.1029/JB078i005p00876>
- Parker RN, Hancox GT, Petley DN (2015) Spatial distributions of earthquake induced landslides and hillslope preconditioning in the northwest South Island, New Zealand. *Earth Surface Dynamics* 3(4): 501-525. <https://doi.org/10.5194/esurf-3-501-2015>
- Panzer F, Halldorsson B, Vogfjörð K (2017) Directional effects of tectonic fractures on ground motion site amplification from earthquake and ambient noise data: a case study in South Iceland. *Soil Dynamics and Earthquake Engineering* 97: 143-154. <https://doi.org/10.1016/j.soildyn.2017.03.024>
- Papadimitriou E, Wen X, Karakostas V, et al. (2004) Earthquake triggering along the Xianshuihe fault zone of western Sichuan, China. *Pure and Applied Geophysics* 161(8): 1683-1707. <https://doi.org/10.1007/s00024-003-2471-4>
- Pedersen H, Brun B, Hatzfeld D, et al. (1994) Ground-motion amplitude across ridges. *Bulletin of the Seismological Society of America* 84(6): 1786-1800.
- Pischiutta M, Salvini F, Fletcher J, et al. (2012) Horizontal polarization of ground motion in the hayward fault zone at Fremont, California: dominant fault-high-angle polarization and fault-induced cracks. *Geophysical Journal International* 188(3): 1255-1272. <https://doi.org/10.1111/j.1365-246X.2011.05319.x>
- Sepulveda SA, William M, Randall WJ, et al (2005) Seismically induced rock slope failures resulting from topographic amplification of strong ground motions: the case of Pacoima Canyon, California. *Engineering Geology* 80: 336-348. <https://doi.org/10.1016/j.enggeo.2005.07.004>
- Sun JB, Yue H, Shen ZG, et al. (2018) 2017 Jiuzhaigou earthquake: a complicated event occurred in a young fault system. *Geophysical Research Letters* 45:1-12. <https://doi.org/10.1002/2017GL076421>
- Spudich P (1996) Directional topographic site response at Tarzana observed in aftershocks of the 1994 Northridge, California, earthquake: Implications for mainshock motions. *Bulletin of the Seismological Society of America* 86(1):193-208.
- Tang C, Ma G, Chang M, et al. (2015) Landslides triggered by the 20 April 2013 Lushan earthquake, Sichuan Province, China. *Engineering Geology* 187: 45-55. <https://doi.org/10.1016/j.enggeo.2014.12.004>
- Tripe R, Kontoe S, Wong TKC (2013) Slope topography effects on ground motion in the presence of deep soil layers. *Soil Dynamics and Earthquake Engineering* 50(7):72-84. <https://doi.org/10.1016/j.soildyn.2013.02.011>
- U S Geological Survey (2013) M 6.6 - 52 km WSW of Linqiong, China. <http://earthquake.usgs.gov/earthquakes/eventpage/usb000gcdd#summary>(accessed on: 2013-04-20)
- U S Geological Survey (2014) M 5.9 - 38km NNW of Kangding, China <https://earthquake.usgs.gov/earthquakes/eventpage/usb000syyo/executive> (accessed on: 2014-11-22).
- Wang YS, He JX, Luo YH (2017) Seismic response of the Lengzhuguan slope during Kangding Ms5.8 earthquake. *Journal of Mountain Science* 14(11): 2337-2347. <https://doi.org/10.1007/s11629-017-4368-1>
- Wang Y, Wang D, Ma X (2012) Slope seismic response monitoring on the aftershocks of the Wenchuan earthquake in the Mianzhu section. *Journal of Mountain Science* 9(4): 523-528. <https://doi.org/10.1007/s11629-012-2179-y>
- Wang Z, Wang J, Chen ZL, et al. (2011) Seismic imaging, crustal stress and gps data analyses: implications for the generation of the 2008 Wenchuan earthquake (M7.9), China. *Gondwana Research* 19(1): 202-212.

- <https://doi.org/10.1016/j.gr.2010.05.004>
- Wu JF (2013) Research on development characteristics and genetic mechanism of the seismic landslide in Dadu River. Chengdu University of Technology, Ph.D thesis. (In Chinese)
- Xu C, Xu X, Shyu J, et al. (2015) Landslides triggered by the 20 April 2013 Lushan, China, Mw 6.6 earthquake from field investigations and preliminary analyses. *Landslides* 12(2): 365-385. <https://doi.org/10.1007/s10346-014-0546-1>
- Xu C, Xu X, Yao X, et al. (2013a) Three (nearly) complete inventories of landslides triggered by the May 12, 2008 Wenchuan mw 7.9 earthquake of china and their spatial distribution statistical analysis. *Landslides* 11(3): 441-461. <https://doi.org/10.1007/s10346-013-0404-6>
- Xu Q, Pei XJ, Huang RQ (2009b) Large-scale landslides induced by Wenchuan earthquake. Science press, Beijing. (In Chinese)
- Xu C, Xu X, Shyu JBH, et al. (2014) Landslides triggered by the 22 July 2013 Minxian–Zhangxian, China, Mw 5.9 earthquake: inventory compiling and spatial distribution analysis. *Journal of Asian Earth Sciences* 92: 125-142. <https://doi.org/10.1016/j.jseaes.2014.06.014>
- Xu X, Gao R, Guo X, et al. (2017). Outlining tectonic inheritance and construction of the Min Shan region, eastern Tibet, using crustal geometry. *Scientific Reports*, 7(1): 13798. <https://doi.org/10.1038/s41598-017-14354-4>
- Xu X, Wen X, Yu G, et al. (2009a) Coseismic reverse-and oblique-slip surface faulting generated by the 2008 Mw 7.9 Wenchuan earthquake China. *Geology* 37(6): 515-518. <https://doi.org/10.1130/G25462A.1>
- Xu X, Wen X, Han Z, et al. (2013b) Lushan M S 7.0 earthquake: A blind reserve-fault event. *Chinese Science Bulletin* 58(28-29): 3437-3443. <https://doi.org/10.1007/s11434-013-5999-4>
- Yi GX, Long F, Wen XZ, et al (2015) Seismogenic structure of the M6.3 Kangding earthquake sequence on 22 Nov. 2014, southwestern China. *Chinese Journal of Geophysics* 058(004):1205-1219. <https://doi.org/10.6038/cjg20150410>
- Zhao B (2020) The Mechanism of Large Earthquake-Triggered Landslides in Area of High Intensity and Deep Canyon of Northwest Sichuan. Chengdu University of Technology. Ph.D thesis. (In Chinese)
- Zhao B, Huang Y, Zhang C, et al. (2015) Crustal deformation on the Chinese mainland during 1998–2004 based on GPS data. *Geodesy and Geodynamics* 6: 7-15. <https://doi.org/10.1016/j.geog.2014.12.006>
- Zhao B, Li W, Wang Y, et al. (2019) Landslides triggered by the Ms 6.9 Nyingchi earthquake, china (18 November 2017): analysis of the spatial distribution and occurrence factors. *Landslides* 16(4): 765-776. <https://doi.org/10.1007/s10346-019-01146-2>
- Zhao B, Wang YS, Feng QQ, et al. (2020) Preliminary analysis of some characteristics of coseismic landslides induced by the Hokkaido Iburi-Tobu earthquake (September 5, 2018), Japan, *Catena* 189: 1-12. <https://doi.org/10.1016/j.catena.2020.104502>
- Zhao B, Wang YS, Luo YH, et al. (2018) Landslides and dam damage resulting from the Jiuzhaigou earthquake (8 August 2017), Sichuan, China. *Royal Society Open Science* 5(3): 171418. <https://doi.org/10.1098/rsos.171418>
- Zhou H, Liu HL, Kanamori H (1983) Source processes of large earthquakes along the Xianshuihe fault in southwestern China. *Bulletin of the Seismological Society of America* 73(2): 537-551.